Special Collection

# Ligand Stabilized $Ni_1$ Catalyst for Efficient CO Oxidation

Minzhen Jian,[a] Chuanlin Zhao,[a] and Wei-Xue Li*[a, b]

Supported single transition metal ($TM_1$) catalysts have attracted broad attention in academia recently. Still, their corresponding reactivity and stability under reaction conditions are critical but have not well explored at the fundamental level. Herein, we use density functional theory calculation and ab initio molecular dynamics simulation to investigate the role of reactants and ligands on the reactivity and stability of graphitic carbon nitride ($g\text{-}C_3N_4$) supported $Ni_1$ for CO oxidation. We find out that supported bare $Ni_1$ atoms are only metastable on the surface and tend to diffuse into the interlayer of $g\text{-}C_3N_4$. Though $Ni_1$ is catalytically active at moderate temperatures, CO adsorption induced dimerization deactivates the catalyst. Hydroxyl groups not only are able to stabilize the supported $Ni_1$ atom, but also increase the reactivity by participating directly in the reaction. Our results provide valuable insights on improving the chemical stability of $TM_1$ by ligands without sacrificing the reactivity, which are helpful for the rational design of highly loaded atomically dispersed supported metal catalysts.

## 1. Introduction

Supported single transition metal ($TM_1$) catalyst has attracted extensive attention among research communities recently, thanks to its high metal atom utilization, markedly different activity and selectivity toward specific reactions.[1] There is increasing evidence showing that it might even have superior performance than its nanoparticle counterparts, by properly choosing metal, support and chemical reaction.[2] However, high reactivity and poor stability are two sides of the same coin for the supported $TM_1$ catalyst owing to its nature of highly unsaturated coordination. So far, various strategies have been developed to improve the stability,[3] such as confining the metal atom geometrically in micro/mesopore space,[4] confining the metal atom in defects[5] and certain hosts[6] with strong metal-support interactions.[7] Nevertheless, the overall performance might still be hindered by diffusion or limited nucleation sites available on the support.[8] Among others, two-dimensional (2D) materials is particularly versatile because of its high surface area, abundant nucleation sites and functional groups.[9] Graphite carbon nitride ($g\text{-}C_3N_4$), consisting of stacked layers of hexagonal building blocks with a high density of pyridinic nitrogen ($N_{py}$) as nucleation sites, is one of the promising 2D support candidates for $TM_1$ catalyst with high metal loading.[10] Therefore, $g\text{-}C_3N_4$ is studied in the present work as the model support for CO oxidation.

Under harsh reaction conditions such as high pressures and elevated temperatures, the supported metal nanoparticles that have strong interaction with reactants/intermediates suffer surface reconstruction, morphology alternation, disintegration and rapid sintering, influencing the catalysts' reactivity and stability dramatically.[11] This happens on the supported $TM_1$ catalysts as well. For example, *In-situ* experiments unveiled the dynamic evolution of the supported $TM_1$ catalysts under reactive atmosphere, where the aggregation of metal atoms was found to be promoted by the presence of reactants such as $H_2$ and CO.[12] But unlike the supported nanoparticles with abundant adsorption sites necessary for hosting reactants and reaction intermediates, only a few sites are available for the supported $TM_1$, thus the corresponding adsorption and reaction mechanism can be quite different.[13] Chemical stability under reaction conditions and competitive adsorption within the catalytic cycle are therefore essential for the supported $TM_1$ catalysts with high reactivity and long durability.

To further improve the stability of the supported $TM_1$ catalyst, ligand could be introduced to form energetically more favorable metal complex on the support. Thermodynamic rule on the rational design of proper reactants/ligands and supports to disintegrate metal nanoparticles into supported metal-reactant complexes has been established in our earlier work.[14] Indeed, a number of highly loaded atomically dispersed supported catalysts stabilized by ligands have been prepared.[15] For instance, Li and co-workers described a facile gas-migration strategy that extracted the atomic copper out of the bulk by ammonia and subsequently trapped the metal complex on the defective nitrogen-rich carbon support to form isolated copper sites.[16] Ding and co-workers demonstrated that supported large nanoparticles of Ru, Rh, Pd, Ag, Ir, Pt can be completely dispersed by reacting with a mixture of $CH_3I$ and CO, then the dispersed metal atom can be immobilized by the oxygen-containing functional group on the carbon support.[17] Nevertheless, the corresponding trade-off of deploying ligands is often the loss of reactivity. Finding the proper ligands able to stabilize the supported $TM_1$ catalysts without sacrificing the reactivity is thus highly desirable but not well explored yet.

[a] *M. Jian, Dr. C. Zhao, Prof. W.-X. Li*
*Department of Chemical Physics*
*School of Chemistry and Materials Science*
*University of Science and Technology of China*
*Hefei, Anhui 230026, China*
*E-mail: wxli70@ustc.edu.cn*
[b] *Prof. W.-X. Li*
*Hefei National Laboratory for Physical Science at the Microscale*
*University of Science and Technology of China*
*Hefei, Anhui 230026, China*

Supporting information for this article is available on the WWW under https://doi.org/10.1002/cphc.202000730

An invited contribution to a Special Collection on Single-Atom Catalysis

To better understand the interplay of reactants/ligands with the supported $TM_1$ catalysts on reactivity and chemical/thermal stability, we present here a systematic density functional theory (DFT) and *ab initio* molecular dynamics (AIMD) study of g-$C_3N_4$ supported $Ni_1$ atom for CO oxidation.[18] Interlayer diffusion and aggregation on the surface in terms of the dimer formation for g-$C_3N_4$ supported $Ni_1$ atom, in the absence and presence of reactants (CO and $O_2$), were investigated to reveal the importance of the chemical stability. Stable co-adsorption structures under a wide range of temperature were investigated, and corresponding reaction mechanisms within the complete catalytic cycle were mapped out. We found out that hydroxyls, one widely present ligand, were able to stabilize the $Ni_1$ atom. Instead of lowering the reactivity, the hydroxyl groups promoted CO oxidation by directly participating in the reaction channel with a lower barrier.

## 2. Results

### 2.1. Structure of $Ni_1$/g-$C_3N_4$ and $Ni_1(OH)_2$/g-$C_3N_4$

Geometric and electronic information based on the optimized structures of bare and hydroxyl stabilized $Ni_1$ on g-$C_3N_4$ is given in Figure 1a, c and 1b, d, respectively. For $Ni_1$/g-$C_3N_4$, the nickel atom anchors at the corner of the six-fold cavity and coordinates with two in-plane $N_{py}$. Both Ni–N bonds are 1.90 Å long (Table 1), rendering a strong Ni binding energy of 3.52 eV with respect to gas phase Ni atom in a neutral state, consistent with previous literature.[19] For $Ni_1(OH)_2$/g-$C_3N_4$, there are two OH groups above the Ni atom, shortening the Ni–N bond lengths slightly to 1.87 Å.

Based on the projected density of states (PDOS) of $Ni_1$/g-$C_3N_4$ and $Ni_1(OH)_2$/g-$C_3N_4$ in Figure 1c and 1d, the Ni 3*d* orbital considerably hybridizes with the N 2*p* band above and below the Fermi level, suggesting a pronounced interaction between $Ni_1$ and $N_{py}$. As shown in the Crystal orbital Hamilton population (COHP) analysis (Figure S1 in the Supporting Information), the splitting of Ni 3*d* orbital results in bonding contribution well below Fermi level and most of anti-bonding interaction above Fermi level. The integrating COHP (ICOHP) averaged over two Ni–N bonds of $Ni_1(OH)_2$/g-$C_3N_4$ is −2.10 eV/bond. By comparison, the ICOHP averaged over two Ni–N bonds of $Ni_1$/g-$C_3N_4$ is −1.76 eV/bond, indicating a weaker binding. Hence, the interaction between Ni atom and g-$C_3N_4$ is strengthened in presence of the hydroxyl ligands.

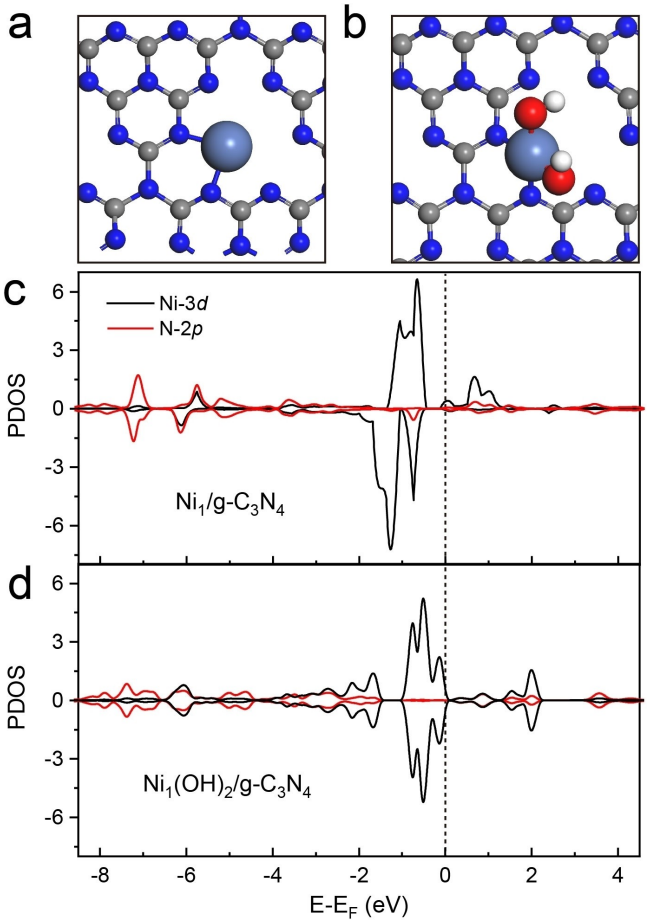


**Figure 1.** Top views of optimized structures of $Ni_1$/g-$C_3N_4$ (a) and $Ni_1(OH)_2$/g-$C_3N_4$ (b). Color code: cyan = Ni, blue = N, gray = C, red = O, and white = H. PDOS of Ni *3d* orbital and N *2p* band in $Ni_1$/g-$C_3N_4$ (c) and $Ni_1(OH)_2$/g-$C_3N_4$ (d). Vertical dashed line represents the Fermi level.

**Table 1.** Calculated overall adsorption energies $\Delta E_{ads}$ (in eV) of reactants/intermediates on $Ni_1$/g-$C_3N_4$ and $Ni_1(OH)_2$/g-$C_3N_4$, absolute value of ICOHP (eV/bond) of Ni–N interactions, Ni–N bond length data (in Å).

| Support | Adsorbate | $\Delta E_{ads}$ | Abs(ICOHP) | Distance Ni–N | Ni–N |
|---|---|---|---|---|---|
| $Ni_1$/g-$C_3N_4$ | none | – | 1.76 | 1.90 | 1.90 |
| | CO | −1.77 | 1.53 | 1.91 | 1.94 |
| | 2CO | −3.20 | 1.05 | 2.00 | 2.02 |
| | 3CO | −4.07 | 0.87 | 2.09 | / |
| | $O_2$ | −2.26 | 2.08 | 1.86 | 1.86 |
| | $CO+O_2$ | −3.02 | 1.79 | 1.92 | 2.24 |
| | $CO+O_2$ (interface) | −3.14 | 2.08 | 1.90 | 1.85 |
| $Ni_1(OH)_2$ /g-$C_3N_4$ | none | – | 2.10 | 1.87 | 1.87 |
| | CO | −0.50 | 1.76 | 1.95 | / |
| | $O_2$ | 0.04 | 1.58 | 1.97 | 1.96 |

### 2.2. Stability

Typical degradation mechanisms for supported $TM_1$ catalysts on stacked g-$C_3N_4$ layers include $TM_1$ diffusion into interlayer space and $TM_1$ aggregation on the surface layer. For the former one, four (meta-)stable structures of $Ni_1$ on the surface layer and interlayers were identified (Figure S2). According to the calculated energetics, $Ni_1$ in the first interlayer of g-$C_3N_4$ is more favorable by 0.72 eV than on the surface layer. This is reasonable because the penetrated $Ni_1$ atom coordinates to two g-$C_3N_4$ layers (surface and subsurface layers), doubling its coordination number compared to $Ni_1$ on the surface layer. Further diffusion into the second interlayer is only modest (an energy gain of 0.26 eV). In other words, bare $Ni_1$ atom tends to

stay in the interlayers of g-$C_3N_4$, a fact of which diminishes the population of the active sites on the surface.[10c]

$Ni_1$ atom on the surface layer can however be stabilized by hydroxyl, a widely present group from environment. For instance, it can be formed by exposing $Ni_1$/g-$C_3N_4$ to a humid environment containing $H_2O$, or mixture of $O_2$ and $H_2$, or $H_2O_2$. Based on our DFT calculations, the dissociative adsorption of $H_2O_2$ on $Ni_1$/g-$C_3N_4$ to form $Ni_1(OH)_2$/g-$C_3N_4$ turns out to be a spontaneous process. Hydroxyl groups on $Ni_1$ turn out to be very stable, because OH disproportion reaction is found to be a significant endothermic process with a reaction energy of 1.49 eV (blue pathway in Figure S3). The Ni hydroxyls system is also stable under $H_2$ atmosphere, according to the non-Horiuti-Polanyi mechanism,[20] forming water and single OH coordinated Ni hydride would require a considerable activation energy barrier of 1.47 eV (red pathway in Figure S3).

The dynamic stability of supported $Ni_1$ and $Ni_1(OH)_2$ catalysts were further examined by AIMD simulation. It is found that with gradual increase of temperature, the bare Ni atom starts to diffuse into the first interlayers at temperature as low as 200 K (Figure 2a). Further diffusion into the second interlayers was not observed even at 500 K, indicating $Ni_1$ atom would enrich below the surface layer, consistent with the abovementioned modest energy gain. While for $Ni_1(OH)_2$, AIMD simulation shows that it remains intact on the surface layer even at T = 500 K (Figure 2b), telling clearly that $Ni_1(OH)_2$ on g-$C_3N_4$ is very stable.

Another stability concern is metal aggregation, the initial step of which is metal dimer formation on the surface layer. Calculated reaction energetics are given in Table S1. Though the formation of $Ni_1$ dimer ($Ni_2$/g-$C_3N_4$) is found to be slightly endothermic (0.06 eV), the corresponding activation energy barrier can be as high as 1.87 eV, which is reasonable because of the strong Ni–N bonds. Without considering Ni penetration into the interlayers, large activation energy barrier required for $Ni_1$ dimer formation implies that high Ni loading on g-$C_3N_4$ is likely to be achieved in the format of atomic dispersion, in-line with experiment.[21] As to $Ni_1(OH)_2$/g-$C_3N_4$, the dimer formation toward $Ni_2(OH)_4$/g-$C_3N_4$ turns out to be thermoneutral as well, with a corresponding activation energy barrier of 1.23 eV. Unlike $Ni_1$ dimer where Ni–Ni bond length is 2.16 Å, the two Ni atoms in $Ni_2(OH)_4$/g-$C_3N_4$ are well separated with a bond distance of 3.06 Å. In other words, no promotion effects by OH groups are found on the aggregation of g-$C_3N_4$ supported $Ni_1$ atom.

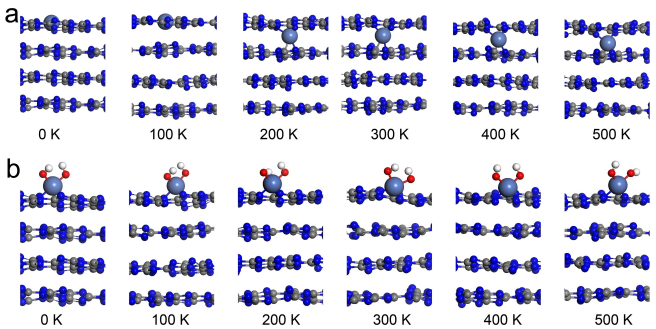


**Figure 2.** Structural evolution of $Ni_1$/g-$C_3N_4$ (a) and $Ni_1(OH)_2$/g-$C_3N_4$ (b) during consecutive temperature ramping process. The snapshots of structures in equilibrium are based on AIMD simulations at 0, 100, 200, 300, 400, 500 K, respectively. Color code: cyan = Ni, blue = N, gray = C, red = O, and white = H.

### 2.3. Adsorption

Molecular adsorptions involved in CO oxidation on various sites of $Ni_1$/g-$C_3N_4$, including adsorption of $O_2$, adsorption of CO up to three molecules, and co-adsorption of CO and $O_2$, were explored. Optimized adsorption structures and corresponding adsorption energies $\Delta E_{ads}$ are summarized in Figure 3 and Table 1. As expected, all of the reactants prefer to bind to the $Ni_1$ atom, rather than g-$C_3N_4$, indicating that the Ni atom, as well as its adjacent interface sites, is the active center for CO oxidation.

As shown in Figure 3a, single CO molecule prefers to adsorb on $Ni_1$ atom by forming a Ni–C bond (1.81 Å). The calculated adsorption energy is −1.77 eV. The strong binding between CO and $Ni_1$ atom indicates that $Ni_1$ might be poisoned by CO at low temperature. Therefore, we also evaluate the cases where multiple CO adsorption on $Ni_1$. The optimized structure for Ni dicarbonyls is shown in Figure 3b with the averaged adsorption energy of −1.60 eV per CO. As to Ni tricarbonyls, the optimized structure is shown in Figure 3c with the averaged adsorption energy of −1.36 eV per CO. The optimal adsorption structure

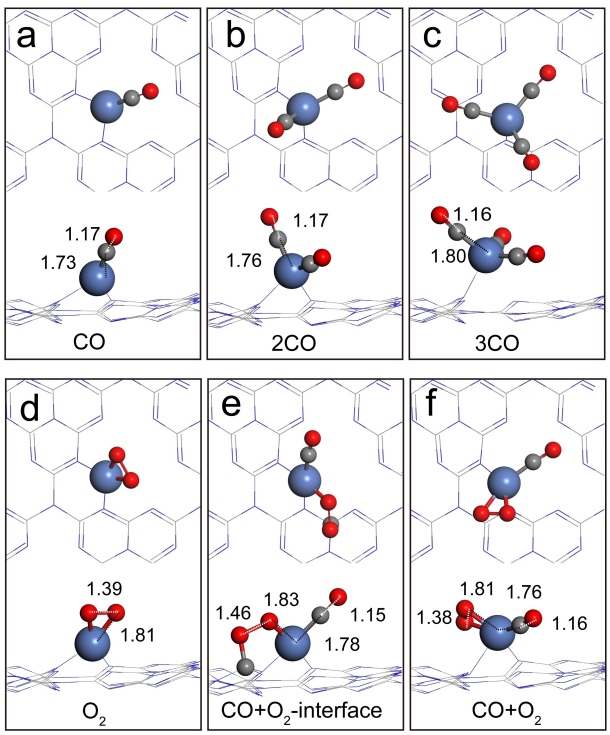


**Figure 3.** Optimized structures for CO (a), 2CO (b), 3CO (c), $O_2$ (d) on $Ni_1$ atom, CO and $O_2$ co-adsorption at the interface site (e) and on $Ni_1$ atom (f) on $Ni_1$/g-$C_3N_4$. Important bond lengths are reported in unit of Å. For clarity purpose, wireframe model of g-$C_3N_4$ was used in this and following figures. Color code: cyan = Ni, gray = C, red = O.

for $O_2$ is shown in Figure 3d, where $O_2$ adsorbs on $Ni_1$ atom by forming two Ni–O bonds (1.81 Å). The O–O bond in the adsorption state is perpendicular to the surface normal. The corresponding adsorption energy is −2.26 eV, which is even stronger than CO adsorption.

For the co-adsorption of CO and $O_2$, two stable adsorption structures are found: (1) CO adsorbs on $Ni_1$ atom and $O_2$ adsorbs at the interface between $Ni_1$ and g-$C_3N_4$ support (Figure 3e), (2) both $O_2$ and CO adsorb on $Ni_1$ atom (Figure 3f). The corresponding adsorption energies are −3.14 eV and −3.02 eV, respectively. Their energy difference is small, implying both $Ni_1$ atom and its adjacent site on g-$C_3N_4$ can participate in the CO oxidation.

As to $Ni_1(OH)_2$/g-$C_3N_4$, optimized structures for CO and $O_2$ adsorption are reported in Figure 4a and 4b, respectively, with detailed information regarding bond distance summarized in Table 1. The CO adsorption structure shows that the bond distance for Ni–C is 1.78 Å, close to the typical bond lengths found in Ni dicarbonyls and tricarbondyls on $Ni_1$/g-$C_3N_4$(1.76 and 1.80 Å, respectively). However, the adsorption energy of CO on $Ni_1(OH)_2$/g-$C_3N_4$ is only −0.50 eV, possibly due to the energy penalty associated with OH ligands rearrangement. Similarly, weak adsorption is found for $O_2$, though the optimized O–O bond length and the O–Ni bond length (1.38 and 1.84 Å, respectively) are close to those of $O_2$ adsorption on $Ni_1$/g-$C_3N_4$ (1.39 and 1.81 Å, respectively).

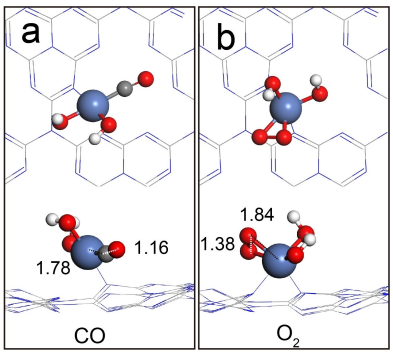


**Figure 4.** Optimized structures for CO (a) and $O_2$ (b) on $Ni_1(OH)_2$/g-$C_3N_4$. Bond lengths are reported in unit of Å. Color code: cyan = Ni, gray = C, red = O, and white = H.

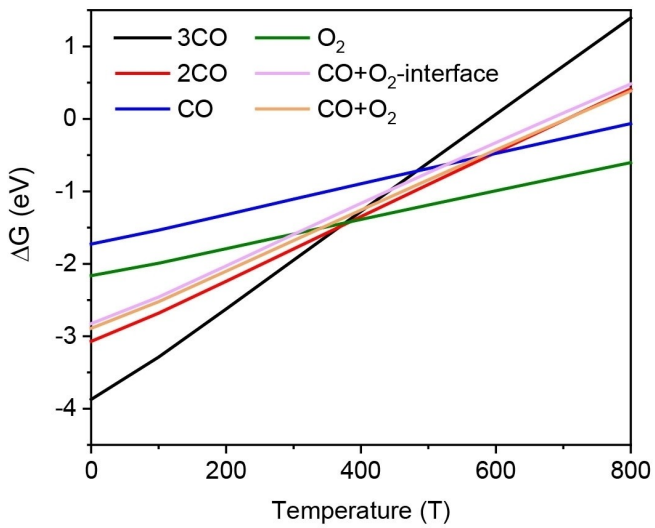


**Figure 5.** Gibbs free energy ΔG of adsorption in eV on the $Ni_1$/g-$C_3N_4$ as a function of temperature, where $P_{CO}$ = 1000 ppm, $P_{O2}$ = 5 % atm. Refer to Figure 3 for the corresponding structures.

In order to figure out favorable adsorption structures under reaction conditions, corresponding Gibbs free energies of adsorption are calculated as a funtion of reaction temperature under typical CO oxidation condition ($P_{CO}$ = 1000 ppm, $P_{O2}$ = 5 % atm[22]), as shown in Figure 5. It is found that at temperature lower than 368 K, Ni tricarbonyls is the most favorable one among all adsorption structures considered on $Ni_1$/g-$C_3N_4$. But there are no extra sites available for $O_2$ adsorption, thus its reactivity toward CO oxidation is low and not considered below. As temperature ramps up, CO starts to desorb and other adsorption structures become competitive including Ni dicarbonyls, co-adsorbed CO and $O_2$, and $O_2$ only. Indeed, at ~368 K, all three adsorption structures have similar Gibbs free energy and therefore likely to co-exist. At higher temperature, $O_2$ only structure on $Ni_1$/g-$C_3N_4$ is the most stable one. CO oxidation based on these adsorption structures are studied below in detail.

### 2.4. CO Oxidation

CO oxidation may proceed through Langmuir-Hinshelwood (LH) mechanism,[23] Eley-Rideal (ER) mechanism,[24] or trimolecular Eley-Rideal (TER) mechanism,[25] depending on reaction conditions. To avoid CO poisoning, reaction has to start above 368 K, where $O_2$ only adsorption on $Ni_1$/g-$C_3N_4$ is favorable for the most part. Gas phase CO approaches adsorbed $O_2$ and the following steps are arranged according to ER mechanism. The reaction energy profile and corresponding reaction intermediates are shown in Figure 6a, with corresponding transition states shown in Figure S5a. Next, CO attacks the adsorbed $O_2$ by forming a C–O bond (ts1). In the final state, the O–O bond scission completes as $CO_2$ forms simultaneously. This step is very exothermic with a reaction energy of −1.93 eV and a highest activation energy barrier of 0.80 eV across the entire reaction energy profile. $CO_2$ binds weakly on the surface ($\Delta E_{ads}$ = −0.33 eV) and therefore can readily desorb once formed. A second CO molecule attacks the remaining O atom on $Ni_1$ to form another $CO_2$. This step is more exothermic with a reaction energy of −2.96 eV, and it only requires a small activation energy barrier of 0.11 eV. Without coadsorbed O, $CO_2$ now binds $Ni_1$ more strongly ($\Delta E_{ads}$ = −0.80 eV). After $CO_2$ desorption, the catalytic cycle becomes complete.

If reaction starts around 368 K, the other adsorption structures including co-adsorbed CO and $O_2$, as well as Ni dicarbonyls can also become competitive. Co-adsorbed CO and $O_2$ is the key characteristic of the LH mechanism. Two co-adsorption structures are identified: (1) both adsorbates on $Ni_1$ atom, (2) CO adsorbate on $Ni_1$ atom, while $O_2$ adsorbate shared by both $Ni_1$ atom and its adjacent C site on the surface of g-

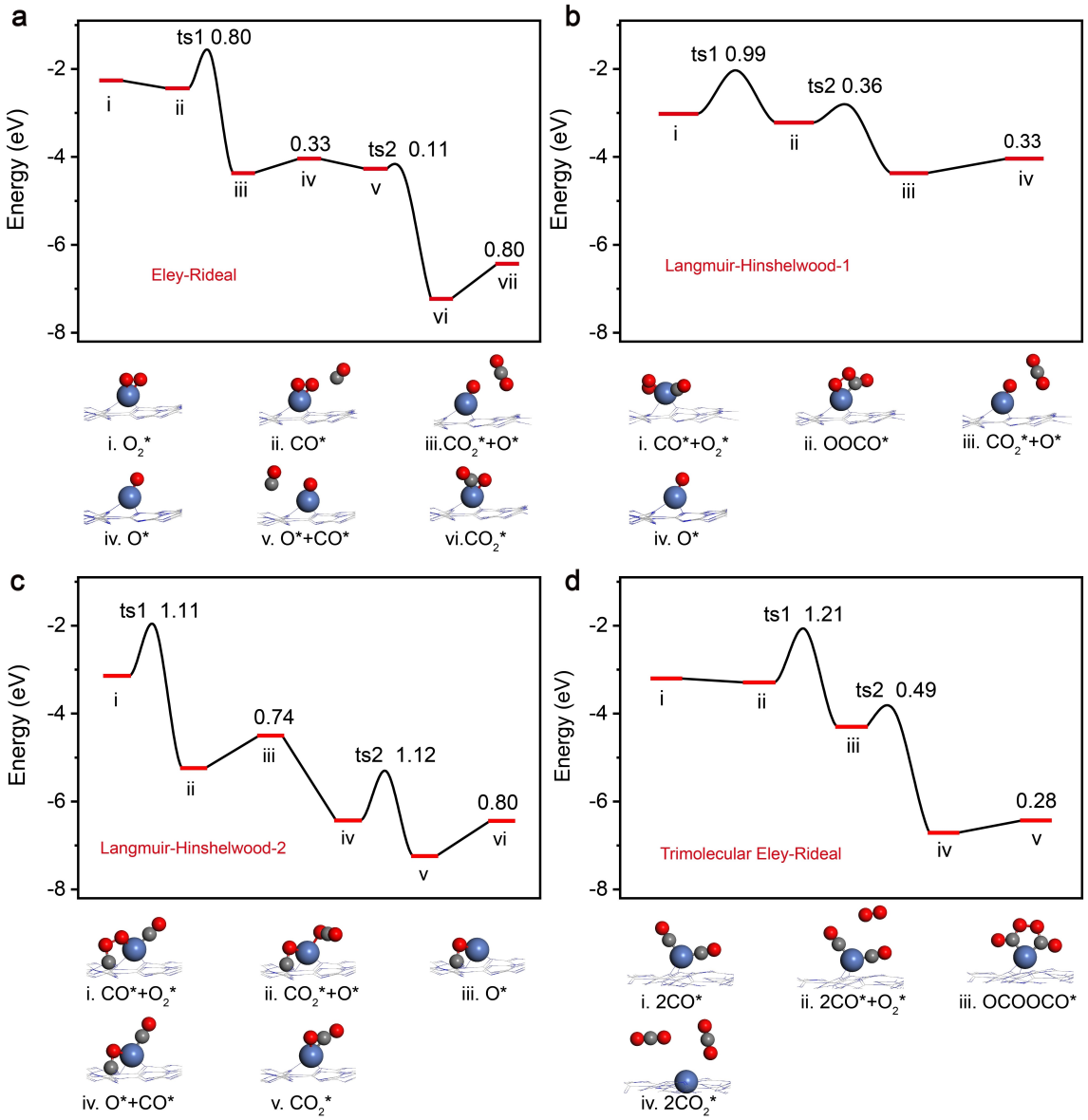


**Figure 6.** Reaction energy profile (top panel) and corresponding reaction intermediates (bottom panel) for CO oxidation on $Ni_1/g\text{-}C_3N_4$: a) ER mechanism, b) LH mechanism-1, c) LH mechanism-2, d) TER mechanism. Activation energy barrier and reaction energy associated with proposed elementary steps are labeled in each panel. Color code: cyan = Ni, gray = C, red = O.

$C_3N_4$. In Scenario 1, CO oxidation starts with one O atom of $O_2$ attacking the C atom of CO, forming a peroxide-like O–O–C–O complex (Figure 6b ii). This step is slightly exothermic by −0.20 eV, but with a noticeable activation energy barrier of 0.99 eV. Next, the O–O bond breaks and $CO_2$ forms simultaneously on $Ni_1$. Afterwards, Ni–C bond breaks and releases the first $CO_2$ to the gas phase with a reaction energy of −1.15 eV and an activation energy barrier of 0.36 eV. The following secondary CO oxidation with the remaining O is the same as the ER mechanism as discussed earlier. In Scenario 2, the O atom bonded with $Ni_1$ atom attacks the C atom of CO, forming $CO_2$ and an O atom was left on the C site of the support (Figure 6c and Figure S5c). This step has a higher activation energy barrier (1.11 eV), compared to the highest activation energy barrier (0.80 eV) reported in the ER mechanism. The secondary CO oxidation starts with migration of the remaining O atom from C site to $Ni_1$ atom, then it attacks the adsorbed CO to form $CO_2$. The activation energy barrier for this step is 1.12 eV, with a reaction energy of −0.81 eV.

The Ni dicarbonyls on $Ni_1/g\text{-}C_3N_4$ can react directly with gas phase $O_2$ via the so-called TER mechanism (Figure 6d). A chelating-like complex of OC–O–O–CO is formed on $Ni_1$ atom. This step is exothermic by −1.01 eV, but with a high activation energy barrier of 1.21 eV. The following step is the dissociation of the O–O bond, it is strongly exothermic with a reaction energy of −2.41 eV and an activation energy barrier of 0.49 eV. Two weakly bonded $CO_2$ molecules can be readily released into gas phase, due to their weak binding with $Ni_1$ ($\Delta E_{ads}$ =

−0.28 eV). Side reactions such as C–C coupling of two carbonyl ligands is very endothermic ($\Delta E_{rxn}$ = 2.89 eV) and therefore excluded. More details are shown in Figure S6.

Due to limited adsorption sites on $Ni_1(OH)_2$/g-$C_3N_4$, only ER mechanism and LH mechanism are considered for CO oxidation, as shown in Figure 7 and Figure S7, respectively. Unlike $Ni_1$/g-$C_3N_4$, the initial step is the formation of a COOH intermediate via coupling OH ligand with the adsorbed CO. The associated activation energy barriers are 0.65 and 0.89 eV for ER and LH mechanism, respectively. As $O_2$ approaches the Ni site, H migrates from COOH to the O atom of the adsorbed $O_2$. Then $CO_2$ migrates onto the surface of the support. This step turns out to be very facile with an activation energy barrier of 0.23 eV. Subsequently, O–O bond breaks and ended up with an oxygen and a renewed OH ligand, both bonded to $Ni_1$ atom. The following step is similar to the secondary CO oxidation as introduced earlier. To close the catalytic cycle, $CO_2$ desorbs from the surface of g-$C_3N_4$ readily with a desorption energy of 0.40 eV. By recalling the highest activation energy barrier associated with CO oxidation on $Ni_1$/g-$C_3N_4$ (Figure 6d) is 1.21 eV, $Ni_1(OH)_2$/g-$C_3N_4$ only requires an activation energy barrier of 0.65 eV.

Side reactions such as water evolution from COOH and OH ligands were considered as well. As shown in Figure S8, the overall reaction is slightly exothermic ($\Delta E_{rxn}$ = −0.37 eV), suggesting a much less thermodynamic driving force than the main reaction pathway described above. The highest activation energy barrier required for the remaining reaction is 0.64 eV, higher than the main reaction ($E_a$ = 0.48 eV). Hence, this side reaction is not competitive, either thermodynamically or kinetically.

## 3. Discussion

For each catalytic reaction, one should consider the adsorption of reactants, subsequent surface reactions, and desorption from the surface, to close the so-called catalytic cycle. In this process, reactants/reaction intermediates induced aggregation might occur simultaneously to deactivate the catalysts. According to the abovementioned results, the $Ni_1$/g-$C_3N_4$ catalyst is inactive below 368 K, because $Ni_1$ is poisoned by three CO molecules. At higher temperature above ~368 K, CO gradually desorbs, so $Ni_1$ reverts to the active site as indicated in Figure 5. On the other hand, ICOHP data show that adsorbed CO weakens the interaction between $Ni_1$ and g-$C_3N_4$ from 1.76 to 1.53 and 1.05 eV/bond (Table S1). As a result, the tendency for aggregation of $Ni_1$ on the support surface increases. This is verified by the calculated dimer formation energy (Figure S3c and d), changing from endothermic of 0.06 eV for $Ni_1$ to exothermic of

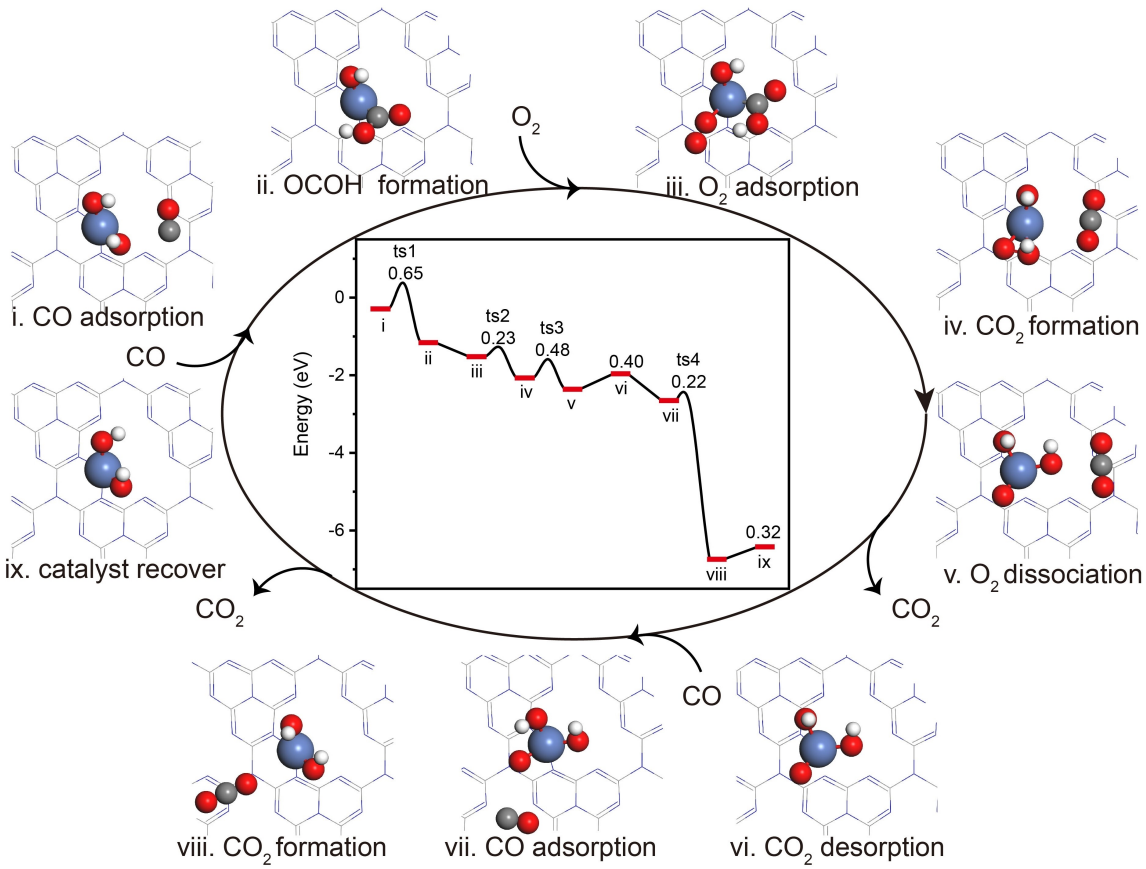


**Figure 7.** Reaction energy profile and corresponding reaction intermediates for CO oxidation on $Ni_1(OH)_2$/g-$C_3N_4$. Activation energy barrier and reaction energy associated with proposed elementary steps are labeled. Color code: cyan = Ni, gray = C, red = O.

−0.43 eV for Ni monocarbonyl ($Ni_1CO_1$). The corresponding activation energy barrier also decreases from 1.87 eV to 1.29 eV. This dimer formation barrier is on par with the activation energy barriers required for CO oxidation on $Ni_1$ via TER and LH mechanism (1.21 and 1.12 eV, respectively). Since CO oxidation on $Ni_1$/g-$C_3N_4$ via TER and LH mechanism occurs preferentially at ~368 K, the above result implies $Ni_1$ catalysts might aggregate simultaneously, gradually losing its catalytic activity. CO induced aggregation and clustering was well documented in literature.[12a,b,26] For oxide supported $TM_1$ atoms, when CO was introduced, formation of the metal-carbonyls and promoted subsequent sintering were obersved by scan tunneling spectroscopy with atomic resolution,[12c,d] which corroborates the present calculation.

At higher temperature where only $O_2$ can stay adsorbed on $Ni_1$, the interaction between $Ni_1$ and g-$C_3N_4$ is increased with ICOHP of −2.08 eV/bond. Along with this, the formation energy of the $Ni_1O_2$ dimer are nearly thermoneutral (0.03 eV, Table S1 and Figure S4e). This tells that adsorption of $O_2$ on $Ni_1$ will not promote the aggregation of $Ni_1$ on g-$C_3N_4$. As a result, CO oxidation on stable $Ni_1O_2$/g-$C_3N_4$ proceeds via ER mechanism has a maximum activation energy barrier of 0.80 eV.

Different from CO, the presence of the hydroxyl group stabilizes supported $Ni_1$ atom, a fact of which is found in previous experimental works[27] and theoretical work.[28] Once $Ni_1(OH)_2$ formed on g-$C_3N_4$, CO oxidation proceeds preferentially via the ER mechanism, and the maximum activation energy barrier is 0.65 eV, which makes it catalytically more active compared to those pathways on $Ni_1$/g-$C_3N_4$ with maximum activation energy barriers ranging above 0.80 eV. Such difference is caused by facile $O_2$ activation enabled by OH ligands. Promotion effects by hydroxyl groups on CO oxidation was found on various supported $TM_1$ catalysts.[29] By comparison, our calculated barriers and overall potential energy surfaces are comparable or even lower than those of $TM_1$ catalysts supported on pyridinic nitrogen graphene,[30] graphene,[31] γ–$Al_2O_3$,[32] and $FeO_x$,[33] suggesting $Ni_1(OH)_2$/g-$C_3N_4$ as a potential efficient catalyst for CO oxidation.

## 4. Conclusions

We performed systematic density functional theory calculation and *ab initio* molecular dynamics simulation, in order to shed light on the role of reactants and ligands on CO oxidation and chemical stability of $Ni_1$ atom supported on g-$C_3N_4$. It is found that the supported bare $Ni_1$ atom is metastable on the surface and tends to diffuse into the interlayer of g-$C_3N_4$. Under moderate temperature, CO and $O_2$ can coadsorb and react to form $CO_2$ on supported $Ni_1$ atom, however, the adsorbed CO promotes the formation of Ni dimer and therefore destabilizes the catalyst. Only at higher temperature, supported $Ni_1$ atom is stabilized by adsorbed $O_2$, which oxidizes CO via Eley-Rideal mechanism. $Ni_1$ atom can be stabilized by hydroxyl groups as $Ni_1(OH)_2$ complex on the surface, free from aggregation on the surface or diffusion into the interlayers of g-$C_3N_4$. Importantly, the presence of the hydroxyl groups increases the activity of CO oxidation by participating in the reaction with a lower activation energy barrier. The present work highlights the interplay of reactants and ligands on reactivity and thermal/chemical stability of supported $TM_1$ catalysts, and calls for careful and thorough investigation in the future.

## Computational Details

Periodic, spin-polarized DFT calculations were implemented in the Vienna *Ab initio* Simulation Package (VASP).[34] The core electrons were represented by projector augmented wave (PAW) method[35] and the Kohn-Sham valence states [Ni(4s3d), O(2s2p), N(2s2p), C(2s2p), H(1s)] were expanded in a plane-wave basis set with a kinetic energy cutoff of 400 eV. The exchange-correlation interaction is described by the optB86b-vdW functional.[36] The convergence threshold for electronic self-consistent interactions is $10^{-4}$ eV. Structural optimization and transition state search were converged to the extent that the maximum residual force was 0.02 eV/Å and 0.05 eV/Å or less in all relaxed degrees of freedom, respectively. Transition states were determined by climbing image nudged elastic band (CI-NEB) method[37] and improved dimer method,[38] then verified to possess only one vibrational mode with a negative curvature in the direction of bond breaking or forming process.

The model catalyst used in our DFT calculations was a single nickel atom supported on a (2×2) supercell of a single layer g-$C_3N_4$, where all the atoms in the supercell including Ni atom were fully relaxed. Surface Brillouin zone was sampled on $\Gamma$-centered (3×3×1) Monkhorst-Pack k-point grid. The vacuum space perpendicular to the surface was 20 Å, which was enough to avoid interaction with adjacent cells. The adsorption energy was calculated as $\Delta E_{ads} = E_{tot} - E_{slab} - \Sigma E_{gas}$, where $E_{tot}$ and $E_{slab}$ refer to the energy of $TM_1$ slab with adsorbates and the energy of the clean $TM_1$ slab, respectively, and $\Sigma E_{gas}$ refers to the sum of the energy of involved gas phase adsorbates in a neutral state. The reaction energy and activation energy barrier were calculated as $\Delta E_{rxn} = E_{FS} - E_{IS}$ and $E_a = E_{TS} - E_{IS}$, where $E_{IS}$, $E_{FS}$ and $E_{TS}$ refer to the energy of the initial state (IS), final state (FS) and corresponding transition state (TS), respectively.

The Gibbs free energy of gas species were corrected as [Eq. (1)]:

$$G(T) = E_{DFT} + ZPE + U(T) - TS(T) + PV \quad (1)$$

Where $E_{DFT}$ is the total energy from DFT at 0 K, ZPE is the zero-point energy. The temperature range was from 0 K to 800 K, the total pressure was 0.1 MPa, the partial pressures of CO and $O_2$ were 0.1 % and 5 %, respectively.

The free energy of adsorbates at temperature T were estimated according to the harmonic approximation -, and the entropy is evaluated using the following equation [Eq. (2-3)]:

$$G(T) = E_{DFT} + ZPE + H(T) - TS(T) \quad (2)$$

$$S(T) = k_B \sum_{i}^{3N} \left[ \frac{\varepsilon_i}{k_B T (e^{\varepsilon_i / k_B T} - 1)} - \ln(1 - e^{-\varepsilon_i / k_B T}) \right] \quad (3)$$

Here, $k_B$ is Boltzmann's constant, N is the number of atoms in the adsorbates.

For AIMD simulation: the g-$C_3N_4$ was modeled by a four-layer slab with a (2×2) supercell. Starting from 0 K, 500 heating steps followed by 500 equilibration steps were set in each temperature ramp that heats the system up by 100 K. A total of five such ramps

were programed till the final temperature of the system reached 500 K. The total time scale was 10 ps given a time step of 2 fs. The COHP method,[39] which reconstructs the orbital-resolved electronic structure via projection of the PAW wave functions onto atomic-like basis functions, was used in chemical bonding analyses as implemented in the LOBSTER package.[40]

## Acknowledgements

*This work was supported by the Key Technologies R&D Program of China (2017YFB0602205, 2018YFA0208603), the National Natural Science Foundation of China (91645202,91945302), and the Chinese Academy of Sciences Key Project (QYZDJ-SSW-SLH054), and used high-performance computational resources provided by University of Science and Technology of China (http://scc.ustc.edu.cn).*

## Conflict of Interest

The authors declare no conflict of interest.

**Keywords:** chemical stability · CO oxidation reactivity · ligand · single-atom catalyst · transition metal

[1] a) A. Wang, J. Li, T. Zhang, *Nat. Chem. Rev.* **2018**, *2*, 65–81; b) B. C. Gates, *Trends Chem.* **2019**, *1*, 99–110; c) Y. Yao, S. Hu, W. Chen, Z.-Q. Huang, W. Wei, T. Yao, R. Liu, K. Zang, X. Wang, G. Wu, W. Yuan, T. Yuan, B. Zhu, W. Liu, Z. Li, D. He, Z. Xue, Y. Wang, X. Zheng, J. Dong, C.-R. Chang, Y. Chen, X. Hong, J. Luo, S. Wei, W.-X. Li, P. Strasser, Y. Wu, Y. Li, *Nat. Catal.* **2019**, *2*, 304–313; d) X.-K. Gu, B. Qiao, C.-Q. Huang, W.-C. Ding, K. Sun, E. Zhan, T. Zhang, J. Liu, W.-X. Li, *ACS Catal.* **2014**, *4*, 3886–3890.

[2] a) N. Cheng, S. Stambula, D. Wang, M. N. Banis, J. Liu, A. Riese, B. Xiao, R. Li, T. K. Sham, L. M. Liu, G. A. Botton, X. Sun, *Nat. Commun.* **2016**, *7*, 1–9; b) S. Wei, A. Li, J. C. Liu, Z. Li, W. Chen, Y. Gong, Q. Zhang, W. C. Cheong, Y. Wang, L. Zheng, H. Xiao, C. Chen, D. Wang, Q. Peng, L. Gu, X. Han, J. Li, Y. Li, *Nat. Nanotechnol.* **2018**, *13*, 856–861.

[3] a) Y. Chen, S. Ji, C. Chen, Q. Peng, D. Wang, Y. Li, *Joule* **2018**, *2*, 1242–1264; b) R. Qin, P. Liu, G. Fu, N. Zheng, *Small Methods* **2018**, *2*, 1700286; c) X. Cui, W. Li, P. Ryabchuk, K. Junge, M. Beller, *Nat. Catal.* **2018**, *1*, 385–397.

[4] a) S. M. J. Rogge, A. Bavykina, J. Hajek, H. Garcia, A. I. Olivos-Suarez, A. Sepúlveda-Escribano, A. Vimont, G. Clet, P. Bazin, F. Kapteijn, M. Daturi, E. V. Ramos-Fernandez, F. X. Llabrés i Xamena, V. Van Speybroeck, J. Gascon, *Chem. Soc. Rev.* **2017**, *46*, 3134–3184; b) P. Serna, B. C. Gates, *Acc. Chem. Res.* **2014**, *47*, 2612–2620.

[5] a) M. J. López, I. Cabria, J. A. Alonso, *J. Phys. Chem. C* **2014**, *118*, 5081–5090; b) X.-K. Gu, C.-Q. Huang, W.-X. Li, *Catal. Sci. Technol.* **2017**, *7*, 4294–4301; c) Z. Chen, E. Vorobyeva, S. Mitchell, E. Fako, M. A. Ortuño, N. López, S. M. Collins, P. A. Midgley, S. Richard, G. Vilé, J. Pérez-Ramírez, *Nat. Nanotechnol.* **2018**, *13*, 702–707; d) S. Wang, J. Li, Q. Li, X. Bai, J. Wang, *Nanoscale* **2020**, *12*, 364–371.

[6] a) R. T. Hannagan, G. Giannakakis, M. Flytzani-Stephanopoulos, E. C. H. Sykes, *Chem. Rev.* **2020**; b) G. Kyriakou, M. B. Boucher, A. D. Jewell, E. A. Lewis, T. J. Lawton, A. E. Baber, H. L. Tierney, M. Flytzani-Stephanopoulos, E. C. H. Sykes, *Science* **2012**, *335*, 1209; c) M. T. Greiner, T. E. Jones, S. Beeg, L. Zwiener, M. Scherzer, F. Girgsdies, S. Piccinin, M. Armbruster, A. Knop-Gericke, R. Schlogl, *Nat. Chem.* **2018**, *10*, 1008–1015.

[7] M. Yang, S. Li, Y. Wang, J. A. Herron, Y. Xu, L. F. Allard, S. Lee, J. Huang, M. Mavrikakis, M. Flytzani-Stephanopoulos, *Science* **2014**, *346*, 1498–1501.

[8] a) B. Qiao, A. Wang, X. Yang, L. F. Allard, Z. Jiang, Y. Cui, J. Liu, J. Li, T. Zhang, *Nat. Chem.* **2011**, *3*, 634–641; b) E. J. Peterson, A. T. DeLaRiva, S. Lin, R. S. Johnson, H. Guo, J. T. Miller, J. Hun Kwak, C. H. F. Peden, B. Kiefer, L. F. Allard, F. H. Ribeiro, A. K. Datye, *Nat. Commun.* **2014**, *5*, 1–11; c) H. Wei, X. Liu, A. Wang, L. Zhang, B. Qiao, X. Yang, Y. Huang, S. Miao, J. Liu, T. Zhang, *Nat. Commun.* **2014**, *5*, 5634.

[9] a) F. Li, G.-F. Han, H.-J. Noh, S.-J. Kim, Y. Lu, H. Y. Jeong, Z. Fu, J.-B. Baek, *Energy Environ. Sci.* **2018**, *11*, 2263–2269; b) Y. Wang, J. Mao, X. Meng, L. Yu, D. Deng, X. Bao, *Chem. Rev.* **2019**, *119*, 1806–1854.

[10] a) X. Huang, Y. Xia, Y. Cao, X. Zheng, H. Pan, J. Zhu, C. Ma, H. Wang, J. Li, R. You, S. Wei, W. Huang, J. Lu, *Nano Res.* **2017**, *10*, 1302–1312; b) H. Yan, H. Cheng, H. Yi, Y. Lin, T. Yao, C. Wang, J. Li, S. Wei, J. Lu, *J. Am. Chem. Soc.* **2015**, *137*, 10484–10487; c) Z. Chen, S. Mitchell, E. Vorobyeva, R. K. Leary, R. Hauert, T. Furnival, Q. M. Ramasse, J. M. Thomas, P. A. Midgley, D. Dontsova, M. Antonietti, S. Pogodin, N. López, J. Pérez-Ramírez, *Adv. Funct. Mater.* **2017**, *27*, 1605785.

[11] a) C. H. Bartholomew, *Appl. Catal. A* **2001**, *212*, 17–60; b) J. A. Moulijn, A. E. van Diepen, F. Kapteijn, *Appl. Catal. A* **2001**, *212*, 3–16.

[12] a) D. Yang, P. Xu, N. D. Browning, B. C. Gates, *J. Phys. Chem. Lett.* **2016**, *7*, 2537–2543; b) L. Liu, D. N. Zakharov, R. Arenal, P. Concepcion, E. A. Stach, A. Corma, *Nat. Commun.* **2018**, *9*, 574; c) G. S. Parkinson, Z. Novotny, G. Argentero, M. Schmid, J. Pavelec, R. Kosak, P. Blaha, U. Diebold, *Nat. Mater.* **2013**, *12*, 724–728; d) R. Bliem, J. E. van der Hoeven, J. Hulva, J. Pavelec, O. Gamba, P. E. de Jongh, M. Schmid, P. Blaha, U. Diebold, G. S. Parkinson, *Proc. Natl. Acad. Sci. USA* **2016**, *113*, 8921–8926.

[13] F. Huang, Y. Deng, Y. Chen, X. Cai, M. Peng, Z. Jia, P. Ren, D. Xiao, X. Wen, N. Wang, H. Liu, D. Ma, *J. Am. Chem. Soc.* **2018**, *140*, 13142–13146.

[14] R. Ouyang, J. X. Liu, W. X. Li, *J. Am. Chem. Soc.* **2013**, *135*, 1760–1771.

[15] a) N. Chaâbane, R. Lazzari, J. Jupille, G. Renaud, E. Avellar Soares, *J. Phys. Chem. C* **2012**, *116*, 23362–23370; -b) J. Wang, M. McEntee, W. Tang, M. Neurock, A. P. Baddorf, P. Maksymovych, J. T. Yates, Jr., *J. Am. Chem. Soc.* **2016**, *138*, 1518–1526; c) J. Jones, H. Xiong, A. T. DeLaRiva, E. J. Peterson, H. Pham, S. R. Challa, G. Qi, S. Oh, M. H. Wiebenga, X. I. Pereira Hernández, Y. Wang, A. K. Datye, *Science* **2016**, *353*, 150–154; d) P. Liu, Y. Zhao, R. Qin, S. Mo, G. Chen, L. Gu, D. M. Chevrier, P. Zhang, Q. Guo, D. Zang, B. Wu, G. Fu, N. Zheng, *Science* **2016**, *352*, 797; e) P. Serna, D. Yardimci, J. D. Kistler, B. C. Gates, *Phys. Chem. Chem. Phys.* **2014**, *16*, 1262–1270.

[16] Y. Qu, Z. Li, W. Chen, Y. Lin, T. Yuan, Z. Yang, C. Zhao, J. Wang, C. Zhao, X. Wang, F. Zhou, Z. Zhuang, Y. Wu, Y. Li, *Nat. Catal.* **2018**, *1*, 781–786.

[17] S. Feng, X. Song, Y. Liu, X. Lin, L. Yan, S. Liu, W. Dong, X. Yang, Z. Jiang, Y. Ding, *Nat. Commun.* **2019**, *10*, 5281.

[18] H. J. Freund, G. Meijer, M. Scheffler, R. Schlogl, M. Wolf, *Angew. Chem. Int. Ed. Engl.* **2011**, *50*, 10064–10094.

[19] a) S. L. Li, H. Yin, X. Kan, L. Y. Gan, U. Schwingenschlogl, Y. Zhao, *Phys. Chem. Chem. Phys.* **2017**, *19*, 30069–30077; b) Z. Chen, J. Zhao, C. R. Cabrera, Z. Chen, *Small Methods* **2018**, *3*, 1800368.

[20] B. Yang, X.-Q. Gong, H.-F. Wang, X.-M. Cao, J. J. Rooney, P. Hu, *J. Am. Chem. Soc.* **2013**, *135*, 15244–15250.

[21] S. Ohn, S. Y. Kim, S. K. Mun, J. Oh, Y. J. Sa, S. Park, S. H. Joo, S. J. Kwon, S. Park, *Carbon* **2017**, *124*, 180–187.

[22] H. Wang, J. X. Liu, L. F. Allard, S. Lee, J. Liu, H. Li, J. Wang, J. Wang, S. H. Oh, W. Li, M. Flytzani-Stephanopoulos, M. Shen, B. R. Goldsmith, M. Yang, *Nat. Commun.* **2019**, *10*, 3808.

[23] L. Molina, B. Hammer, *J. Catal.* **2005**, *233*, 399–404.

[24] W. An, Y. Pei, X. C. Zeng, *Nano Lett.* **2008**, *8*, 195–202.

[25] K. Mao, L. Li, W. Zhang, Y. Pei, X. C. Zeng, X. Wu, J. Yang, *Sci. Rep.* **2014**, *4*, 5441.

[26] a) C. Dessal, T. Len, F. Morfin, J.-L. Rousset, M. Aouine, P. Afanasiev, L. Piccolo, *ACS Catal.* **2019**, *9*, 5752–5759; b) S. Duan, R. Wang, J. Liu, *Nanotechnology* **2018**, *29*, 204002.

[27] a) H. Jeong, G. Lee, B. S. Kim, J. Bae, J. W. Han, H. Lee, *J. Am. Chem. Soc.* **2018**, *140*, 9558–9565; b) Z. J. Zhao, T. Wu, C. Xiong, G. Sun, R. Mu, L. Zeng, J. Gong, *Angew. Chem. Int. Ed. Engl.* **2018**, *57*, 6791–6795; c) M. A. Brown, Y. Fujimori, F. Ringleb, X. Shao, F. Stavale, N. Nilius, M. Sterrer, H.-J. Freund, *J. Am. Chem. Soc.* **2011**, *133*, 10668–10676.

[28] R. Addou, T. P. Senftle, N. O'Connor, M. J. Janik, A. C. T. van Duin, M. Batzill, *ACS Nano* **2014**, *8*, 6321–6333.

[29] a) L. Cao, W. Liu, Q. Luo, R. Yin, B. Wang, J. Weissenrieder, M. Soldemo, H. Yan, Y. Lin, Z. Sun, C. Ma, W. Zhang, S. Chen, H. Wang, Q. Guan, T. Yao, S. Wei, J. Yang, J. Lu, *Nature* **2019**, *565*, 631–635; b) C. Wang, X.-K. Gu, H. Yan, Y. Lin, J. Li, D. Liu, W.-X. Li, J. Lu, *ACS Catal.* **2016**, *7*, 887–891; c) L. Nie, D. Mei, H. Xiong, B. Peng, Z. Ren, X. I. P. Hernandez, A. DeLaRiva, M. Wang, M. H. Engelhard, L. Kovarik, A. K. Datye, Y. Wang, *Science* **2017**, *358*, 1419–1423; d) G. Chen, Y. Zhao, G. Fu, P. N. Duchesne, L. Gu, Y. Zheng, X. Weng, M. Chen, P. Zhang, C. W. Pao, J. F. Lee, N. Zheng, *Science* **2014**, *344*, 495–499.

[30] M. Wang, Z. Wang, *RSC Adv.* **2017**, *7*, 48819–48824.

[31] X.-Y. Xu, J. Li, H. Xu, X. Xu, C. Zhao, *New J. Chem.* **2016**, *40*, 9361–9369.

[32] T. Yang, R. Fukuda, S. Hosokawa, T. Tanaka, S. Sakaki, M. Ehara, *ChemCatChem* **2017**, *9*, 1222–1229.
[33] J.-X. Liang, X.-F. Yang, A. Wang, T. Zhang, J. Li, *Catal. Sci. Technol.* **2016**, *6*, 6886–6892.
[34] a) G. Kresse, J. Furthmüller, *Comput. Mater. Sci.* **1996**, *54*, 11169; b) G. Kresse, J. Furthmüller, *Comput. Mater. Sci.* **1996**, *6*, 15–50.
[35] G. Kresse, D. Joubert, *Phys. Rev. B* **1999**, *59*, 1758.
[36] J. Klimeš, D. R. Bowler, A. Michaelides, *Phys. Rev. B* **2011**, *83*, 195131.
[37] a) G. Henkelman, H. Jónsson, *J. Chem. Phys.* **2000**, *113*, 9978–9985; b) G. Henkelman, B. P. Uberuaga, H. Jónsson, *J. Chem. Phys.* **2000**, *113*, 9901–9904.
[38] J. Kastner, P. Sherwood, *J. Chem. Phys.* **2008**, *128*, 014106.
[39] a) R. Dronskowski, P. E. Blochl, *J. Phys. Chem.* **1993**, *97*, 8617–8624; b) V. L. Deringer, A. L. Tchougreeff, R. Dronskowski, *J. Phys. Chem. A* **2011**, *115*, 5461–5466.
[40] a) S. Maintz, V. L. Deringer, A. L. Tchougreeff, R. Dronskowski, *J. Comput. Chem.* **2013**, *34*, 2557–2567; b) S. Maintz, V. L. Deringer, A. L. Tchougréeff, R. Dronskowski, *J. Comput. Chem.* **2016**, *37*, 1030–1035.

Manuscript received: August 25, 2020
Revised manuscript received: September 15, 2020
Version of record online: October 16, 2020